
X-Ray observations of a subhalo associated with the NGC 4839 group infalling toward the Coma cluster

Toru SASAKI¹ Kyoko MATSUSHITA¹ Kosuke SATO¹ and Nobuhiro OKABE^{2,3}

¹Department of Physics, Tokyo University of Science, 1-3 Kagurazaka, Shinjuku-ku, Tokyo 162-8601 Japan

²Department of Physical Science, Hiroshima University, 1-3-1 Kagamiyama, Higashi-Hiroshima, Hiroshima 739-8526, Japan

³Hiroshima Astrophysical Science Center, Hiroshima University, Higashi-Hiroshima, Kagamiyama 1-3-1, 739-8526, Japan

*E-mail: j1213703@gmail.com; matusita@rs.kagu.tus.ac.jp

Received ; Accepted

Abstract

We report *Suzaku* X-ray observations of the dark subhalo associated with the merging group of NGC 4839 in the Coma cluster. The X-ray image exhibits an elongated tail toward the southwest. The X-ray peak shifts approximately $1'$ away from the weak-lensing mass center toward the opposite direction of the Coma cluster center. We investigated the temperature, normalization, pressure, and entropy distributions around the subhalo. Excluding the X-ray tail, the temperature beyond the truncation radius is 8–10 keV, which is two times higher than that of the subhalo and the X-ray tail. The pressure is nearly uniform excluding southern part of the subhalo at two times of the truncation radius. We computed the gas mass within the truncation radius and the X-ray tail. While the gas fraction within the truncation radius is about 5 times smaller than that of regular groups, the gas mass in the subhalo and the X-ray tail to weak-lensing mass ratio is consistent with that of regular groups. Assuming the infall velocity, 2000 km s^{-1} , the ram pressure is 1.4 times greater than gravitational force per unit area. Assuming the Kelvin-Helmholtz instabilities, the total lost mass is approximately $3 \times 10^{11} M_{\odot}$. If this gas had originally been within the truncation radius, the gas mass fraction of the subhalo would have been comparable with those of regular groups before infalling to the Coma cluster.

Key words: galaxies: clusters: individuals(Coma cluster, the NGC 4839 group) - galaxies: clusters: intracluster medium - X-rays:galaxies:clusters

1 Introduction

Galaxy clusters have formed through mergers of clusters and/or accretions of smaller groups and galaxies. X-ray observations have revealed features such as shocks, cold fronts, and gas stripping tails, around accreting galaxy groups to clusters (e.g., Markevitch et al. 2000; Markevitch et al. 2002;

Markevitch & Vikhlinin 2007; Russell et al. 2010; Ghizzardi et al. 2010; Russell et al. 2014; Eckert et al. 2014; Ichinohe et al. 2015). Shock fronts are expected to occur in front of a merging subhalo and to heat the intracluster medium (ICM). Radio relics, which are diffuse synchrotron radio emissions, are thought to be tracers of shock structures (Ferrari et al. 2008)

and recent *XMM-Newton*, *Chandra* and *Suzaku* observations have found jumps in temperature across these radio relics (e.g., Finoguenov et al. 2010; Akamatsu & Kawahara 2013; Itahana et al. 2015; Akamatsu et al. 2015). Markevitch et al. (2000) found an edge in surface brightness where the temperature jumped, and the gas pressure across the edge was continuous. Such a feature is called a ‘cold front’, and is caused by gas sloshing when a minor merger oscillates the cool dense core of a cluster (e.g., Ascasibar & Markevitch 2006). In addition, the accreting galaxies and groups experience the stripping of gas by ram pressure (e.g., Gunn & Gott 1972). The gas stripped from the accreting objects looks like a tail structure in the X-ray band.

Weak-lensing measurement is a direct, powerful technique to probe dark matter distribution of clusters without resting any assumptions of dynamical states. Since the lifetime of the dark matter subhalos is longer than that of gas subhalos (Tormen et al. 2004), weak-lensing enables us to measure the dark matter mass of the subhalos whose interaction triggers the gas features discussed above. Therefore, a joint weak-lensing and X-ray study is powerful to understand cluster mergers. To date, several joint studies of major mergers have revealed the interaction between ICM and the dark matter subhalo (Clowe et al. 2006; Okabe & Umetsu 2008; Okabe et al. 2011; Okabe et al. 2015; Medezinski et al. 2015). However, joint studies on minor mergers are not yet sufficient. A recent weak-lensing study (Okabe et al. 2014; see also Okabe et al. 2010) for the Coma cluster detected 32 small subhalos whose mass was greater than $\sim 3 \times 10^{12} h^{-1} M_{\odot}$. The ratio between the subhalo mass and the virial mass reaches down to a few 10^{-3} . Detections of such small subhalos was achievable by the large apparent size, because the cluster is very close to us.

There are four massive subhalos whose masses are greater than $\sim 1 \times 10^{13} M_{\odot}$, and labeled “ID 1”, “ID 2”, “ID 9”, and “ID 32” in Okabe et al. (2014). The massive subhalo signals excluding the “ID 2” in the Coma cluster, as well as stacked signals from all subhalos, were well represented with a truncated Navarro-Frenk-White (NFW) mass model (Navarro et al. 1995) as expected from a tidal destruction model (Okabe et al. 2014). These subhalos excluding the “ID 9” were observed with *Suzaku* (Sasaki et al. 2015). While excess X-ray emission from the “ID 1” and “ID 32” subhalos was detected, the “ID 2” did not have excess X-ray emission. The gas mass to weak-lensing mass ratios of the “ID 1” and “ID 32” subhalos were 0.001, which is one to two orders of magnitude smaller than those of regular groups. This supports that ram pressure with typical infall velocities can strip significant amounts of gas from the infalling subhalos.

In this paper, we describe the thermodynamics around the third massive subhalo “ID 9” whose mass and truncation radius (r_t) are $(1.58 \pm 0.26) \times 10^{13} M_{\odot}$ and $3.43^{+0.28}_{-0.47}$, respectively, as detected by weak-lensing analysis (Okabe et al. 2014). The

subhalo “ID 9” is associated with the NGC 4839 group, which is the most famous merging substructure in the Coma cluster. It is located at a projected distance of approximately $50'$ ($\sim r_{500}^1$). The NGC 4839 group has an X-ray tail toward the southwest or opposite to the direction of the Coma cluster center (Briel et al. 1992). With *XMM-Newton*, Neumann et al. (2001) reported complex temperature structures around the NGC 4839 group, with indications of a bow shock and of ram pressure stripping. At the southwest of the NGC 4839 group, a radio relic was discovered around the virial radius of the Coma cluster (Ballarati et al. 1981). The X-ray observations found that there is temperature discontinuity at the relic, which corresponds to a shock with the Mach number ~ 2 (Ogrea & Brügggen 2013; Akamatsu et al. 2013).

We summarize the observation logs and data reductions in section 2. Section 3 shows an X-ray image around subhalo “ID 9” with the mass distribution derived from weak-lensing analysis, and results of spectral analysis. We discuss thermodynamics around the massive subhalo in section 4.

In this paper, we use $\Omega_{m,0} = 0.27$, $\Omega_{\Lambda} = 0.73$, and $H_0 = 70 \text{ km s}^{-1} \text{ Mpc}^{-1}$. The redshift of the Coma cluster is $z = 0.0231$ (Struble & Rood 1999). At this redshift, $1'$ corresponds to 28.9 kpc. The solar abundance table is given by Lodders (2003). Unless noted otherwise, the errors are in the 68% confidence region for the single parameter of interest.

2 Observations and data reduction

We analyzed *Suzaku* data of six pointing observations around the NGC 4839 group (labeled as the “ID 9” subhalo in Okabe et al. 2014). The observation logs are summarized in table 1. The X-ray Imaging Spectrometers (XIS) data were only used in this study. The XIS was operated in the normal clocking mode (8 s exposure per frame) with 3×3 or 5×5 editing mode. The data reduction criteria were the same as those of Sasaki et al. (2015). In addition, we excluded flickering pixels from our analysis². The reduction and analysis were performed with HEASOFT version 6.16. We applied the latest calibration database version 2015-March-12.

3 Analysis and results

3.1 X-ray image of the subhalo

Figure 1 (a) shows the XIS image in the 0.5-5.0 keV energy range around the subhalo “ID 9”. Here, the differences in exposure time and instrumental background were corrected by the “xisexpmapgen” and “xisnxbgen” Ftools tasks, while the vignetting effect was not. We also obtained *XMM-Newton* pub-

¹ r_{500} is the radius within which the mean density of the cluster is 500 times the critical density of the universe.

² http://www.astro.isas.jaxa.jp/suzaku/analysis/xis/nxb_new/

Table 1. *Suzaku* observation logs around the NGC 4839 group.

Field name	Sequence Number	Date-Obs.*	(R.A., decl.) [†] (J2000.0)	Exposure [‡] (ksec)
ID9 East	808020010	2013-Jun-09T13:12:43	12 ^h 58 ^m 01 ^s .7, 27°22′08″.0	16.2
ID9 North	806047010	2011-Jun-23T12:58:52	12 ^h 57 ^m 44 ^s .5, 27°43′35″.8	6.6
ID9 West	802047010	2007-Dec-02T10:08:56	12 ^h 57 ^m 01 ^s .4, 27°34′17″.0	23.9
ID9 South	802048010	2007-Dec-04T04:47:49	12 ^h 56 ^m 06 ^s .0, 27°25′30″.7	29.3
ID 2	808021010	2013-Jun-10T00:39:15	12 ^h 55 ^m 55 ^s .3, 27°45′17″.6	23.7
ID 1	808022010	2013-Jun-10T14:12:00	12 ^h 55 ^m 28 ^s .0, 27°31′00″.1	18.4

* Start date of the observation written in the event FITS files as DATE-OBS keyword.

[†] The nominal position of the observation written in the event FITS files as RA_NOM and DEC_NOM keywords.

[‡] After data screening.

lic image in 0.4-1.3 keV from “*XMM-Newton Science data images*”³. Figure 2 (a) is the *XMM-Newton* image of the Coma cluster with mass contour (Okabe et al. 2014). The subhalo “ID 9” is highlighted in figure 2 (b).

The X-ray peak derived from the *XMM-Newton* image, which is spatially coincident with the NGC 4839 galaxy, is shifted approximately 1′ (0.3 r_t) away from the weak-lensing mass center toward the opposite direction of the Coma cluster center. The position uncertainty of weak-lensing mass center is $\sim 20''$ because of a finite sample of background galaxies. Since the X-ray peak is determined with an accuracy of a few arcsecond, the two peaks are offset. The *XMM-Newton* image shows that at the head of the NGC 4839 group, the surface brightness has an edge like structure. The bright X-ray tail is elongated toward the southwest direction or the outskirts of the Coma cluster, out to approximately 6 r_t , ~ 600 kpc from the X-ray peak. In addition to the tail, *Suzaku* image shows an extended excess X-ray emission around the weak-lensing mass contours from the northeast to the southwest direction. The apparent size of the excess is about several times of r_t .

3.2 Spectral modeling for the foreground, background and ICM components

To investigate the excess emission associated with the subhalo, “ID 9”, we included the ICM emission in the spectral model. The ICM emission was modeled by a single thermal component with APEC plasma code (Smith et al. 2001) for the ICM emission ($apec_{ICM}$) modified by the photoelectric absorption model, $phabs$, for the Galactic absorption ($phabs_{GAL}$). We adopted the azimuthally-averaged radial profiles of the ICM temperature and normalization derived by Simionescu et al. (2013), which are plotted in Figure 3. Here, the southwest direction, which includes the subhalo “ID 9”, was excluded. In this paper, the normalization is defined as following formula; $Norm = \int n_e n_H dV / [4\pi (1+z)^2 D_A^2] \times 10^{-14} \text{ cm}^{-5} / (20^2 \pi) \text{ arcmin}^{-2}$ (see Ishisaki et al. 2007 for detail). In the

³ http://heasarc.gsfc.nasa.gov/docs/xmm/xmm_gal_science.html

Table 2. Regional notations

Area name	Angle (degree)	radius (r_t)
Center	0-360	0-1
NWW	20-48	1-2, 2-3, 3-4
NW	48-94	1-2, 2-3, 3-4
NE	94-140	1-2, 2-3, 3-4
E	140-228	1-2, 2-3, 3-4
S	228-305	1-2, 2-3, 3-4
SW	305-340	1-2, 2-3, 3-4
Tail	340-380, 315-355*	1-2, 2-3, 3-4, 4-6, 6-8

* For 4 – 6 r_t and 6 – 8 r_t regions.

following spectral fits, we restricted the ICM parameters within the error ranges of the azimuthally-averaged profiles at the same distance from the cluster center (hereafter, *Default*-case). The abundance of the ICM was fixed at 0.3 solar (Simionescu et al. 2013). We also fitted the spectra by changing the abundance of the ICM to be 0.2 solar, and obtained almost the same temperatures and normalizations.

We assumed the X-ray foreground and background emissions to be composed of the local hot bubble (LHB), milky way halo (MWH), and cosmic X-ray background (CXB). The LHB and MWH are modeled by unabsorbed and absorbed APEC model, $apec_{LHB}$ and $phabs_{GAL} \times apec_{MWH}$, respectively. The CXB was assumed as a absorbed power-law whose photon index was fixed at 1.4 (e.g., Kushino et al. 2002). The parameters of $apec_{LHB}$, $apec_{MWH}$, and $powerlaw_{CXB}$ were restricted within the error range estimated from 110′-130′ regions of the Coma cluster by Sasaki et al. (2015).

3.3 Spectral fittings of the excess emission

We extracted the spectra within a circular region whose radius is the same as r_t , 3.43′, centered on the weak-lensing signal peak, (R.A., Decl.) = (12^h57^m31^s.44, 27°29′34″.80). As shown in figure 4, beyond r_t , we used annular regions whose radii were

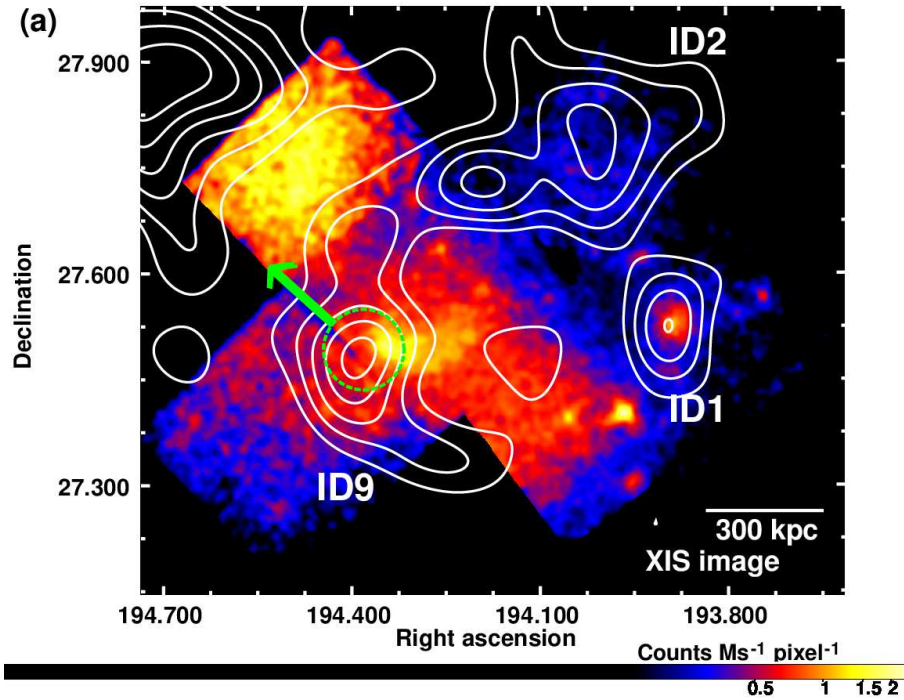


Fig. 1. *Suzaku* XIS mosaic image around subhalo “ID 9” in the 0.5–5.0 keV energy band. While the exposure time and instrumental background were corrected, the effect of the vignetting were not corrected. The image was smoothed by a Gaussian of $\sigma = 16$ pixels $\approx 17''$. The numbers below the color bars have units of counts $\text{Ms}^{-1} \text{pixel}^{-1}$. The white contour shows the mass distribution in a linear scale derived from weak-lensing analysis (Okabe et al. 2014). The dashed circle indicates the r_t of the subhalo “ID 9”. The arrow indicates the direction toward the Coma cluster center.

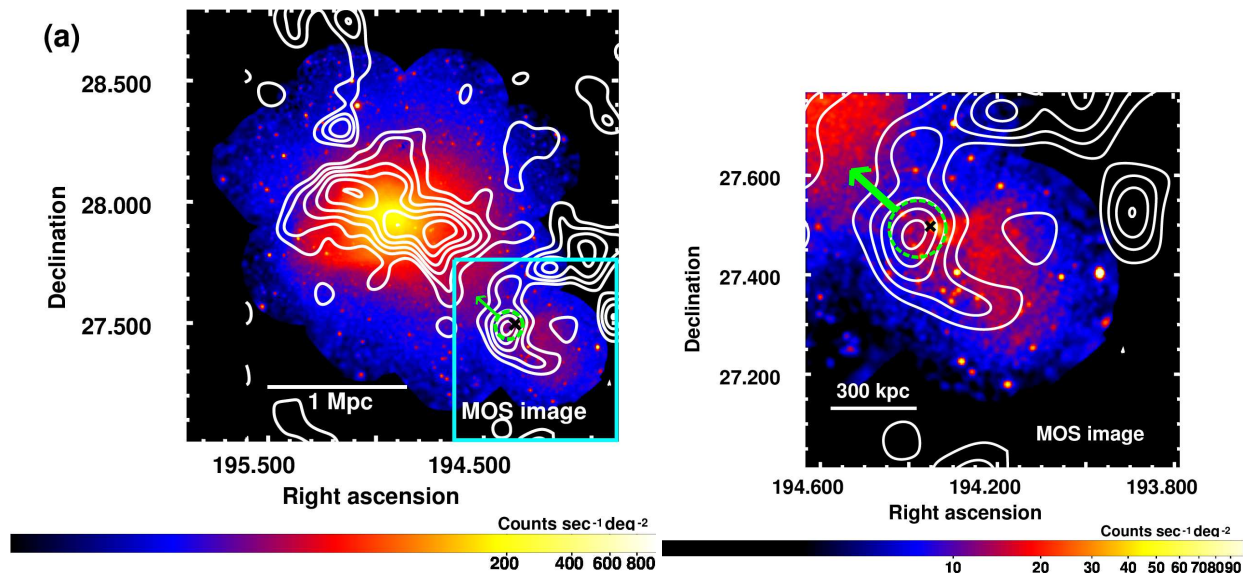


Fig. 2. (a) *XMM-Newton* public image of the Coma cluster⁴. The energy band is 0.4–1.3 keV. The image was smoothed by a Gaussian of $\approx 12''$. The cross indicates the position of the NGC 4839 obtained from NED. The notations of contour, circle, and arrow are the same as the figure 1. (b) The same figure as figure (a), but around subhalo “ID 9” highlighted by cyan box in figure (a).

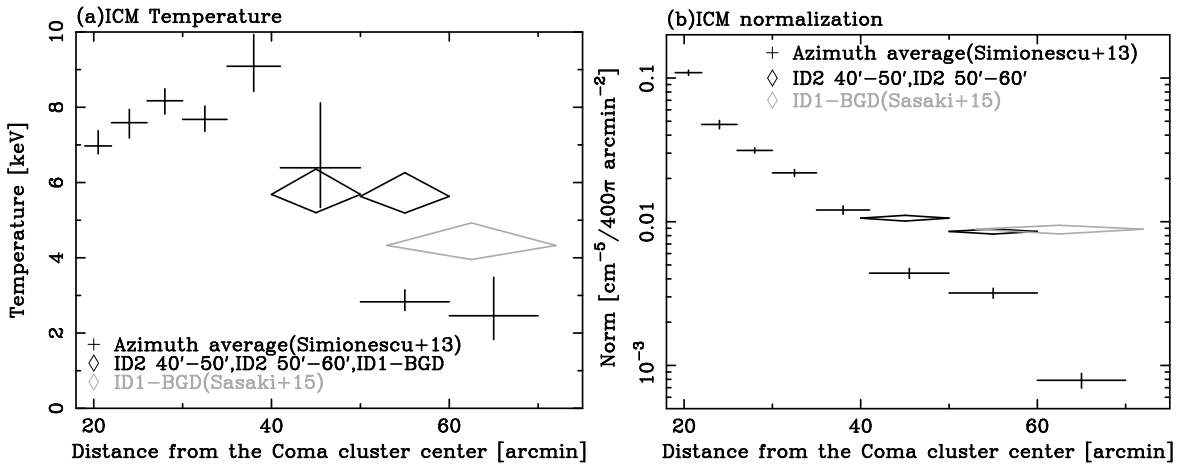


Fig. 3. The radial profiles of (a) temperature and (b) normalization of the ICM. The normalization is defined as $Norm = \int n_e n_H dV / [4\pi(1+z)^2 D_A^2] \times 10^{-14} \text{ cm}^{-5} / (20^2 \pi) \text{ arcmin}^{-2}$. The crosses show the azimuthal average profiles (Simionescu et al. 2013) excluding the southwest direction which includes the subhalo, “ID 9”. The black diamonds are those derived from the regions of “ID2 within 50’”, “ID2 beyond 50’”. Those derived from the “ID1-BGD” region are plotted with light-gray diamonds (Sasaki et al. 2015).

1 – 2 r_t , 2 – 3 r_t , and 3 – 4 r_t and divided into 7 sectors labeled as “NW”, “NE”, “E”, “S”, “SW”, “Tail”, and “NWW”. In addition, we extracted the spectra from annular regions whose radii were 4 – 6 r_t and 6 – 8 r_t for “Tail” sector. The angles of the each sector and the radii of the annular regions are summarized in table 2. Using the “wavdetect” tool in CIAO package, we searched for point sources in the *Suzaku* XIS image. Circular regions with 1’ radius around the detected point sources were excluded from the spectral analysis. The exclusion radii were 1.5’ and 2’ for the point source flux brighter than $2 \times 10^{-13} \text{ erg s}^{-1} \text{ cm}^{-2}$ and $4 \times 10^{-13} \text{ erg s}^{-1} \text{ cm}^{-2}$ in 2–10 keV energy range, respectively. The calibration corners are also removed from the spectral analysis.

We added an absorbed thermal model, $phabs_{GAL} \times apec_{subhalo}$, to the spectral model used for the background regions, and fitted the spectra around the subhalo. As a result, the spectra were fitted by following formula; $constant \times (apec_{LHB} + phabs_{GAL} \times (apec_{MWH} + apec_{ICM} + apec_{subhalo} + powerlaw_{CXB}))$. The abundance of $apec_{subhalo}$ was fixed at 0.3 solar. All spectral fitting was performed in 0.7–8.0 keV (BI) and 0.8–8.0 keV (FI) energy range. As shown in figure 5 and figure 15–20 in Appendix, the spectra were well-represented by our spectral-modeling.

3.4 Temperature and normalization profiles of the subhalo component

The radial profiles of the temperatures along the individual directions and temperature map are shown in the top panel of figure 6 and figure 7 (a), respectively. The temperature within r_t is 5 keV, While the temperatures at 1 – 2 r_t in the “NE”, “NW”, “SW”, and “S” sectors increase up to 8–10 keV, these in the other sectors are 4–7 keV. The temperature profile of the “Tail”

sector is flat at ~ 5 keV up to 4 r_t , and about ~ 3 keV beyond this radius. In the “E” sector, the temperature is likely to be decreasing with the radius, albeit with large error bars. Neumann et al. (2001) studied the temperature structure around the NGC 4839 group, and obtained $8.0_{-2.4}^{+5.0}$ keV (90% confidence level) in 0.5–1.5 r_t of the “SW” sector. Akamatsu et al. (2013) also reported the temperature profiles of southwest and north areas of the NGC 4839 group. We note that southwestern and northern areas in earlier works in Akamatsu et al. (2013) coincides with the “Tail” and “SW” sectors and the “NE”, “NW” and “NWW” sectors respectively. Therefore, our spatial resolution of temperature measurements is finer than those of Akamatsu et al. (2013). They reported the temperature profiles of southwest areas within 10’ ($\sim 3 r_t$) from the NGC 4839 group. Our profiles in “Tail” region are consistent with that of southwest area in Akamatsu et al. (2013). Using the same data with our work, the best-fit temperature of a north area derived Akamatsu et al. (2013) was ~ 7 keV, and consistent with our results.

The radial profiles and map of normalizations are shown in the bottom panels of figure 6 and figure 7 (b), respectively. We find that the normalizations in the “NE” sector are roughly constant. Conversely, the normalizations of the sectors other than “SW” decreased with radius. In particular, the gradient of the “S” and “E” sectors were steeper than that of the other sectors. The normalization in the “Tail” sector smoothly decreases with the radius out to 6 r_t , and the normalization of 6 – 8 r_t is two times lower than that of 4 – 6 r_t .

3.5 Systematic uncertainties by the ICM subtraction

The radial profiles of the temperature and normalization of the ICM in the Coma cluster show significant azimuthal variations (Simionescu et al. 2013). As plotted in Figure 3, the ICM

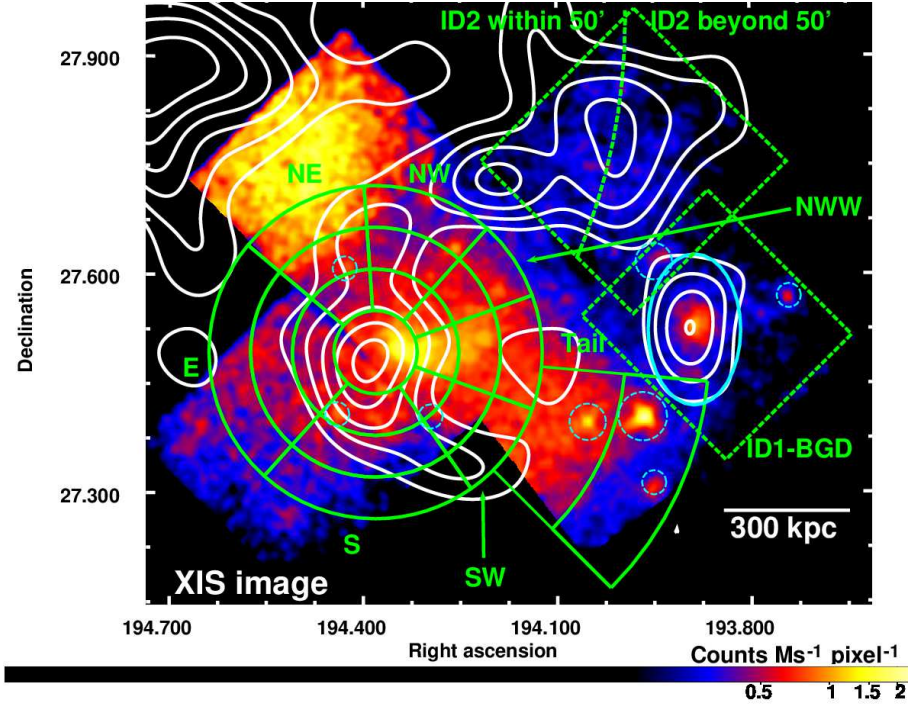


Fig. 4. The same figure as figure 1, but overlaid with the regions from which we extracted the spectra. The green dashed regions are the areas for which background was estimated. Note that the radius of the innermost circle is equal to the truncation radius of the subhalo. The cyan dashed circles indicate the point sources excluded from the analysis. The cyan solid ellipse shows the subhalo “ID 1”, which was excluded from the spectral analysis for the “ID1-BGD” region by Sasaki et al. (2015).

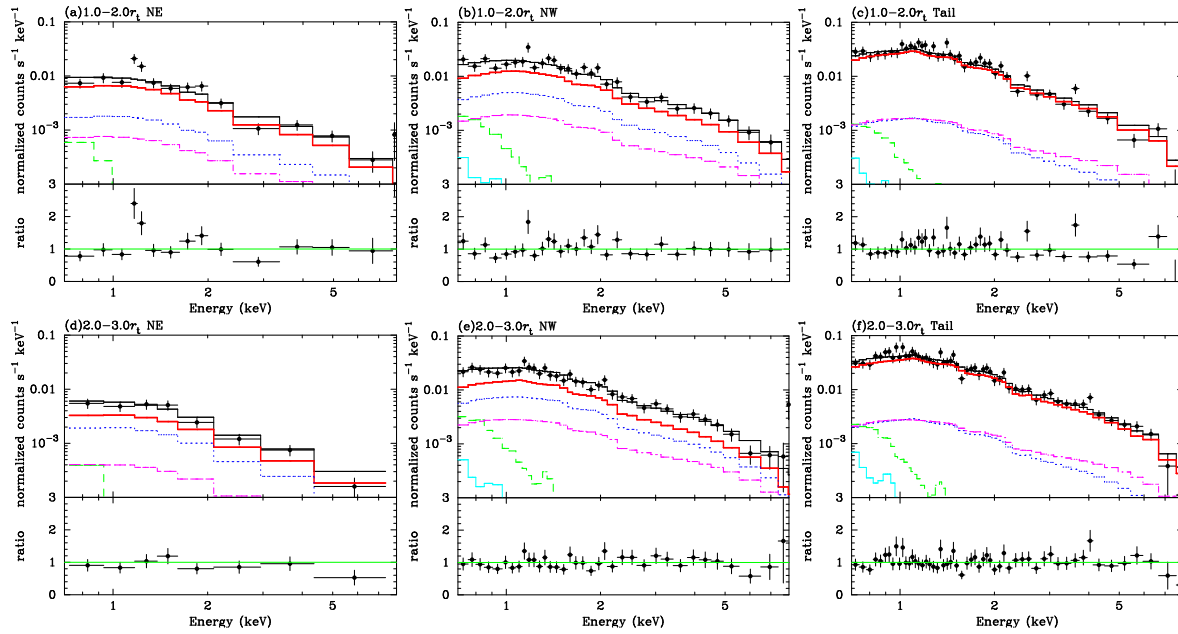


Fig. 5. (Top panels) The panels from left to right panels are the “NE”, “NW”, and “Tail” sectors with $1 - 2 r_t$ annular region. The spectra were rebinned here for display purposes only. Upper panels show the NXB subtracted XIS 1 spectra (black crosses). The subhalo component is plotted as a (red) bold line. The ICM, CXB, LHB, and MWH components are indicated by (blue) dotted, (magenta) dash-dotted, (cyan) thin, and (green) dashed lines, respectively. The lower panels show the data-to-model ratios. (Bottom panels) The same as the top panels, but the radius is $2 - 3 r_t$.

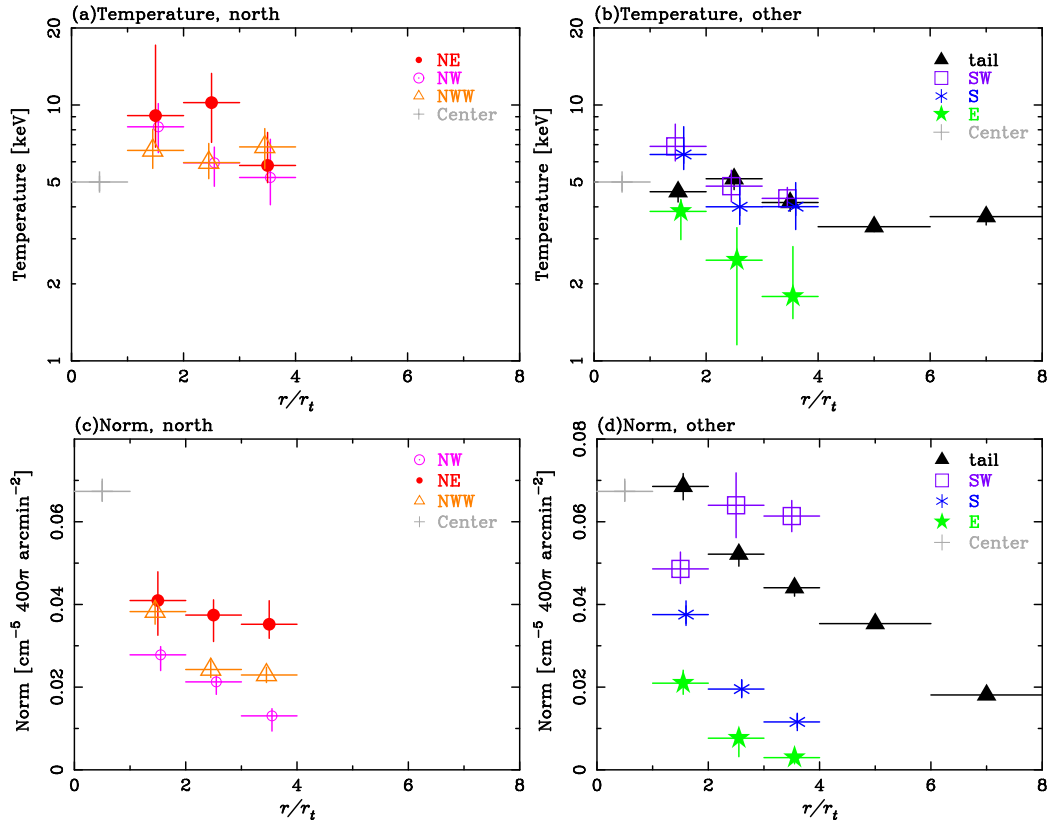


Fig. 6. (Top panels) Radial temperature profiles derived from subhalo-model fitting. The left and right panels are the northern part of the subhalo (labeled “NE”, “NW”, and “NWW”) and the other direction, respectively. The marks and color notations are shown in the figures. The radius is normalized by r_t . The vertical lines indicate the error range of the fitting result of the “ID9-BGD” region. (Bottom panels) The same as the top panels, but showing normalization profiles.

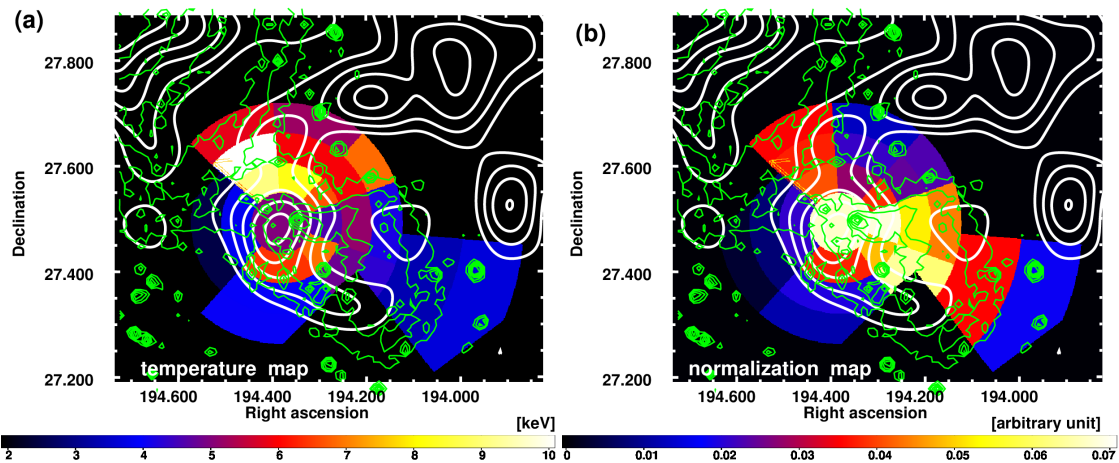


Fig. 7. (a) Temperature map and (b) normalization map of the subhalo component. The unit of normalization is arbitrary. The thin and bold contours are surface brightnesses obtained from the XMM-Newton public image in figure 2 (a) and mass contour from weak-lensing analysis (Okabe et al. 2014), respectively.

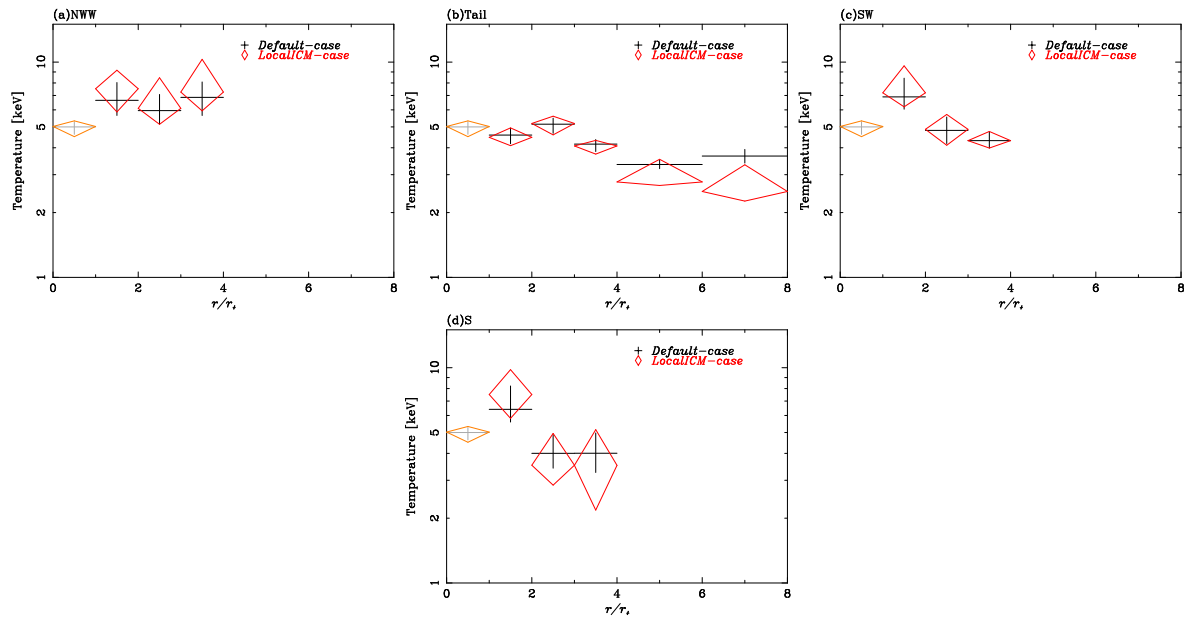


Fig. 8. Radial temperature profiles of the subhalo component along each direction. The radius is normalized by r_s . The crosses are the results derived from the ICM parameters estimated from Simionescu et al. (2013) (*Default-case*). The diamonds indicate the results with ICM parameters with *LocalICM-case*. For details, see text.

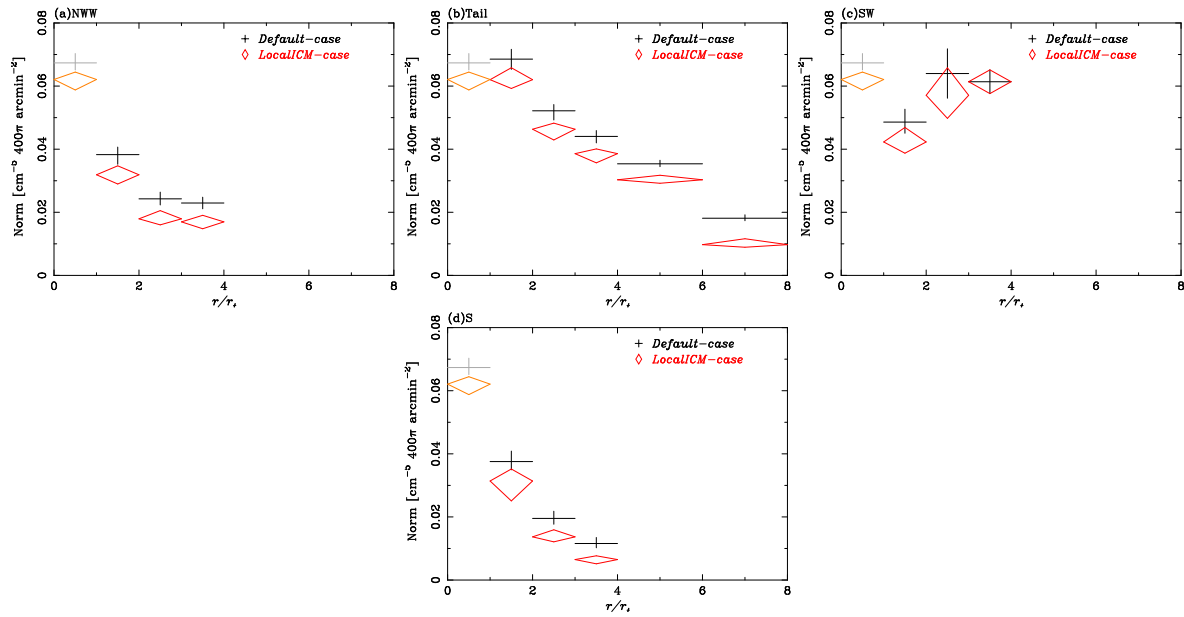


Fig. 9. The same as figure 8, but for normalization profiles.

Table 3. Fitting results of the ICM component at the *Suzaku* BGD regions.

Field name	Distance* [']	kT [keV]	Normalization [†]
ID2 within 50'	40' – 50'	$5.45_{-0.46}^{+0.61}$	$10.6_{-0.69}^{+0.47}$
ID2 beyond 50'	50' – 60'	$5.43_{-0.48}^{+0.67}$	$8.31_{-0.34}^{+0.58}$

* Distance from the Coma cluster center.

† The normalization is defined as $Norm = \int n_e n_H dV / [4\pi(1+z)^2 D_A^2] \times 10^{-17} \text{ cm}^{-5} / (20^2 \pi) \text{ arcmin}^{-2}$.

around the subhalo "ID 1" derived by Sasaki et al. (2015) (the ID1-BGD region plotted in Figure 4), has significantly higher temperature and normalization than the azimuthally averaged values by Simionescu et al. (2013). Therefore, to study the local enhancement of the subhalo, "ID 9" compared to the surrounding ICM component, we extracted the spectra from the observation of subhalo "ID 2", which shows no significant excess emission as reported by Sasaki et al. (2015). As shown in figure 4, the field-of-view of the "ID 2" observation was divided into two regions; within and beyond 50' from the center of the Coma cluster, (R.A., Decl.) = (12^h59^m44^s.81, 27°56'49".92). These regions were labeled as "ID2 within 50'" and "ID2 beyond 50'". We fitted the spectra extracted from these two regions using the same background and foreground parameters described in section 3.2. Here, the ICM abundance was fixed at 0.3 solar. We also fitted the spectra by changing the abundance of the ICM to be 0.2 solar, and obtained almost the same temperatures and normalizations. The resultant ICM parameters are summarized in table 3 and shown in figure 3. The derived temperatures and normalizations from "ID2" regions smoothly connect the azimuthally-averaged profiles at 40' from the cluster center. However, beyond this radius, the temperatures and normalizations from the "ID2" and "ID1-BGD" regions are nearly flat with radius, and significantly higher than the azimuthally averaged profiles.

We fitted the subhalo "ID 9" spectra which were extracted from the regions beyond 40' from the cluster center in the same way as in section 3.3, but using the ICM parameters derived from the two "ID 2" and "ID 1" observations (hereafter *LocalICM*-case). Figure 8 and 9 show the derived temperatures and normalizations, respectively, for the sectors "NWW", "Tail", "SWW", and "S" and the "Center" region, which are located beyond 40' from the cluster center. The temperatures did not change within statistic error ranges excluding 6–8 r_t in the "Tail" sector. The normalizations for the *LocalICM*-case are slightly smaller than these with *Default*-case in figure 9. The difference is caused by the increase the ICM normalizations of *LocalICM*-case, which is several times higher than that of *Default*-case as shown in figure 3 (b).

4 Discussion

We analyzed the *Suzaku* data from the six pointing observations around a massive subhalo "ID 9" detected by the weak-lensing survey (Okabe et al. 2014), which is associated with the NGC 4839 group. We first discuss the pseudo-pressure and pseudo-entropy profiles around the subhalo in section 4.1. Section 4.2 discusses the possible shock heating at the high-temperature region. We compare the X-ray properties with those of regular groups in section 4.3. Section 4.4 discusses the effect of ram pressure stripping.

4.1 Pressure and entropy distributions around the subhalo

To investigate the thermodynamical structure, we study the pseudo-pressure and pseudo-entropy distributions around the subhalo. Since the normalization derived from spectral fitting is proportional to the square of the electron density⁵, we obtained the density profiles using the square root of the normalizations. Therefore, thermal pressure, defined as $P = kT n_e$, is converted to $P \propto kT norm^{0.5}$. The resultant pseudo-pressure map and profiles of each sector are shown in figures 10 and 11, respectively. The pseudo-pressure is nearly continuous around the subhalo ($< 3 r_t$). Beyond r_t , the pseudo-pressure distributions of the "NE" and "NWW" sectors are nearly flat. In contrast, at $2 r_t$ of the "S" and "E" sectors, the pseudo-pressure is discontinuous; pressures of $2 - 3 r_t$ in the "S" and "E" sectors are approximately half of those of $1 - 2 r_t$, respectively. In the "E" sector, however, the temperature at $2 r_t$ is not discontinuous due to large error range. The pressure profile of the "Tail" sector smoothly decreases with radius up to $8 r_t$.

The entropy, defined as $K = kT n_e^{-2/3}$, is a useful parameter for investigating the thermodynamics of galaxy clusters. We computed the pseudo-entropy defined as $K \sim kT norm^{-1/3}$. The resultant pseudo-entropy map and profiles are shown in figures 12 and 13, respectively. The entropy in the "Tail" regions are almost constant and equal to that in the "Center" region. The entropy in the "NE", "NW", and "NWW" sectors are relatively higher than that in the "Center". Beyond $2 r_t$, the pseudo-entropy in the "S" and "SW" sector are comparable with that in the "Tail" sector. Removal of the low entropy gas due to ram-pressure creates a low entropy tail. In contrast, the "NE" and "NW" sectors have 2-3 times higher entropies than that in the "Center". Entropy in the "NWW" sectors also is about two times higher than that in the "Center".

⁵ The definition of the normalization is summarized in Xspec manual page; <https://heasarc.gsfc.nasa.gov/xanadu/xspec/manual/XSmodelApec.html>

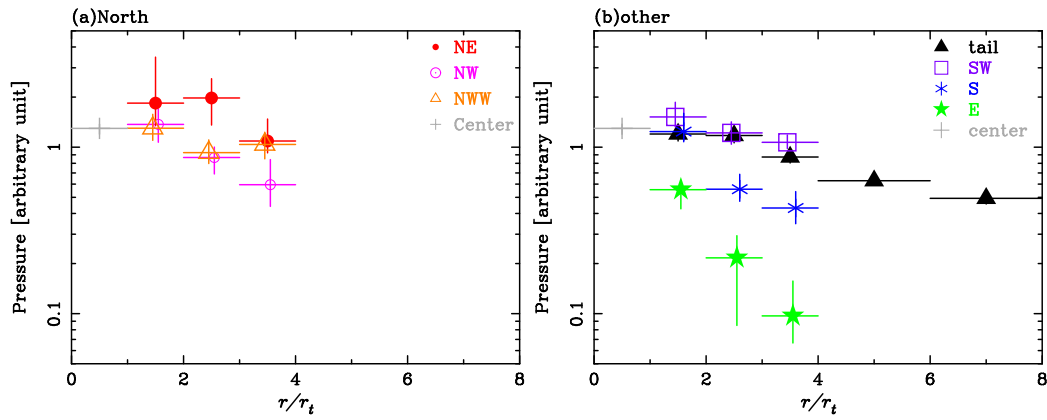


Fig. 11. Radial pseudo-pressure profiles of the subhalo component. Panel (a) and (b) are the northern parts and the other directions, respectively. The radius is normalized by r_t .

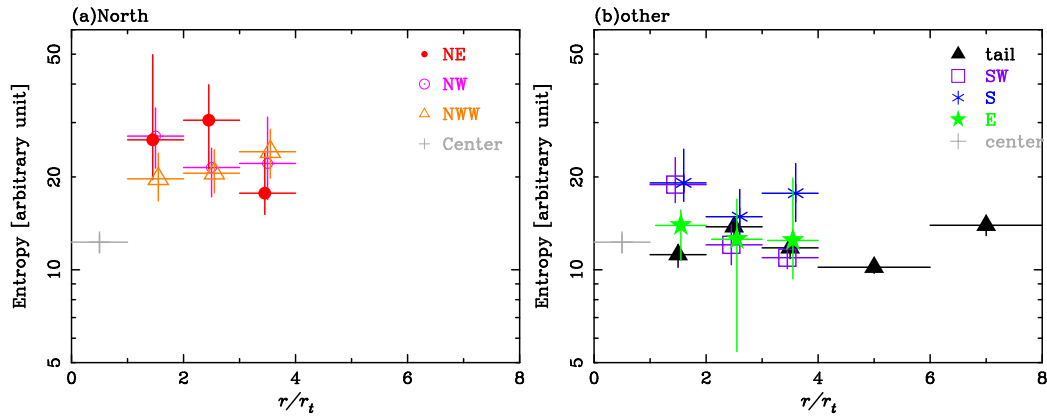


Fig. 13. Same as figure 11, but for pseudo-entropy profiles.

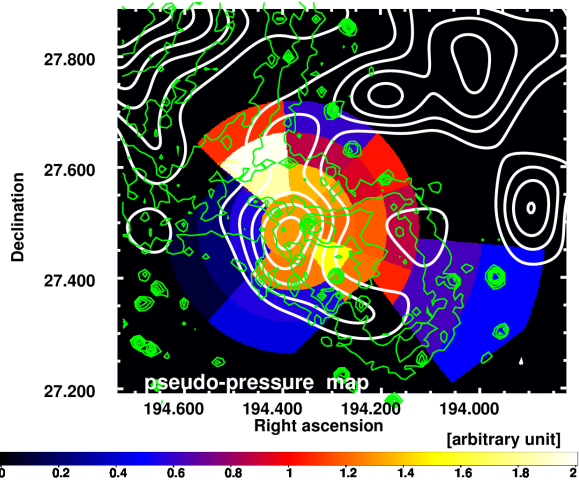


Fig. 10. Pseudo-pressure map of the subhalo component. The units of the pressure map are arbitrary. The thin and bold contours are surface brightness from the *XMM-Newton* and mass contour from weak-lensing analysis (Okabe et al. 2014), respectively.

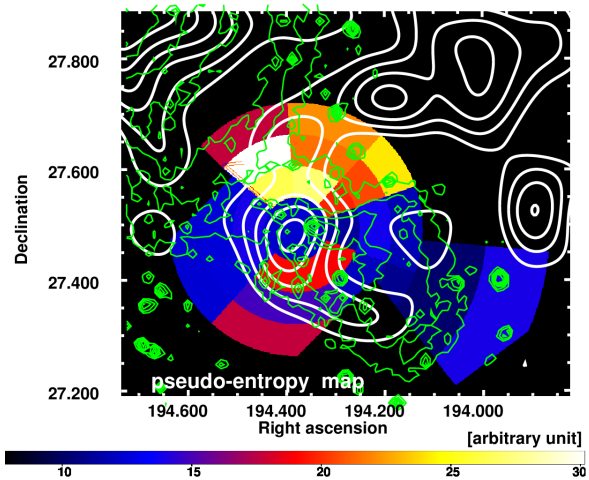


Fig. 12. Same as figure 10, but for pseudo-entropy profiles.

4.2 Possible shock heating around the subhalo

In order to study the possible shock heating, we calculated the Mach number \mathcal{M} under the Rankine-Hugoniot condition using the following formula;

$$\frac{T_2}{T_1} = \frac{5\mathcal{M}^4 + 14\mathcal{M}^2 - 3}{16\mathcal{M}^2}. \quad (1)$$

Here, the subscripts 1 and 2 indicate pre-shock and post-shock values, respectively. We have assumed a specific heat ratio of $\gamma = 5/3$.

Akamatsu et al. (2013) found temperature jump at the radio relic caused by the accretion of the NGC 4839 group. The Mach number of the shock at the radio relic is about 2. At the $2 r_t$ in the ‘‘S’’ sector, we found the temperature jump from ~ 7 keV to ~ 4 keV. Adopting the temperatures of $1 - 2 r_t$ and $2 - 3 r_t$ in the ‘‘S’’ sector, the resultant Mach number is $1.60^{+0.64}_{-0.48}$. At the $3 r_t$ in the ‘‘NE’’ sector, there is also possible temperature jump although the statistic error is too large to make sure. Adopting the temperature of $2 - 3 r_t$ and $3 - 4 r_t$, the Mach number is $1.74^{+0.68}_{-0.82}$. Due to high-temperature and complex emissions of the excess structure, we could not detect the shock heated gas significantly. Although our results have large error bars, there is no discrepancy with Akamatsu et al. (2013). In order to detect the shock heated gas clearly, hard X-ray spectrometers like *NuSTAR* should observe around the NGC 4839 groups.

4.3 Comparison of X-ray properties with other regular groups and clusters

To compare the X-ray properties with those of the regular groups and clusters, we first calculated the mean density within r_t . The resultant value is approximately 30000 times greater than the critical density of the Universe. With Chandra’s results (Vikhlinin et al. 2006), we computed the $kT - M$ and $M_{gas} - M$ relations at the same overdensity as that of the subhalo.

In figure 14 (a), the $kT - M$ relation of the subhalo associated with the NGC 4839 group is compared with that of the other subhalos and regular groups. In contrast to the other two subhalos reported by Sasaki et al. (2015), if we adopt the temperature within r_t , the $kT - M$ relation of the subhalo is consistent with that of the regular groups.

To estimate the gas mass of the excess emission of the subhalo, ‘‘ID 9’’, we estimated the electron density for each spectral fitting region. Within the truncation radius, we assumed a spherical region with uniform electron density. The geometries of the other regions were approximated as truncated cones whose radii are the same as those of individual regions. Integrating the derived electron densities, we computed the gas mass of the subhalo. The gas mass within r_t , $M_{gas,Center}$, is approximately $1.1 \times 10^{11} M_\odot$. The estimated total gas mass up to $8 r_t$ was $M_{gas,Center} + M_{gas,Tail}(< 8 r_t) = (10.7 \pm 0.3) \times 10^{11} M_\odot$. To

study the uncertainties of the geometry, we also computed the electron density and gas mass assuming with spherical shells. The gas masses of each sector with spherical shell are few tens of percents larger than these assuming cones.

The resultant $M_{gas} - M$ relations for the ‘‘Center’’ within r_t , $M_{gas,Center} - M_{WL}$, is shown in figure 14 (b). The gas fraction within r_t , or the ratio of $M_{gas,Center}(< r_t)$ to the weak-lensing mass by Okabe et al. (2014), is about 5 times lower than those of the regular galaxy groups and clusters. For comparison, we also plotted the same relation for the other two subhalos derived from Sasaki et al. (2015). The gas mass fractions of these two subhalos are much lower than those of regular galaxy groups, and most of the gas may have already been stripped away. Therefore, the most of the gas associated with the group has now been stripped. Assuming that the stripped gas was now in the ‘‘Tail’’ sector, we computed again the gas fraction in the ‘‘Tail’’ sector by changing the radius. As a result, the fraction out to $8 r_t$ in the ‘‘Tail’’ sector, $M_{gas,Center}(< r_t) + M_{gas,Tail}(< 8 r_t)$ to the weak-lensing mass ratio, is comparable within the dispersion of that of regular groups.

4.4 Ram pressure stripping

The thermodynamic properties around the subhalo associated with the NGC 4839 group indicate the gas stripping. When the ram pressure is greater than the gravitational storing force per area, the gas associated with the subhalo is effectively stripped. To investigate the ratio between ram pressure and gravitational force per unit area ratio, we adopted the same equation described in Sasaki et al. (2015):

$$\begin{aligned} Ratio &= \frac{P_{ram}}{F_{grav}/Area} \\ &= 0.8 \left(\frac{r}{100 \text{ kpc}} \right)^4 \left(\frac{n_{e,ICM}}{10^{-4} \text{ cm}^{-3}} \right) \left(\frac{M_{subhalo}}{10^{13} M_\odot} \right)^{-1} \\ &\quad \left(\frac{M_{gas,subhalo}}{10^{11} M_\odot} \right)^{-1} \left(\frac{v}{2000 \text{ km s}^{-1}} \right)^2 \end{aligned} \quad (2)$$

Here, the $n_{e,ICM}$, v_{gal} , r , $M_{subhalo}$, and $M_{gas,subhalo}$ are the electron density of the ICM, velocity of the subhalo, radius, the mass of subhalo, and gas mass of the subhalo, respectively. The normalization of the ICM component of the ‘‘ID2 within 50’’ region is approximately 4 times greater than those at a similar distance from the cluster center in other directions (Simionescu et al. 2013). Therefore, we assumed that the $n_{e,ICM}$ around the subhalo was $2 \times 10^{-4} \text{ cm}^{-3}$, and two times greater than that of the other arms. The M_{gas} and $M_{subhalo}$ were adopted as the gas mass and weak-lensing masses within r_t . The infall velocity of $\sim 2000 \text{ km s}^{-1}$ was computed from the NFW profile for the main halo derived from Okabe et al. (2014). Adopting 5 keV and a Mach number $1.73^{+0.25}_{-0.16}$ at $2 r_t$ in the ‘‘S’’ sector, the velocity calculated from the Mach number, $2000 \pm 300 \text{ km s}^{-1}$, was comparable with the infall velocity. At r_t , the ratio was

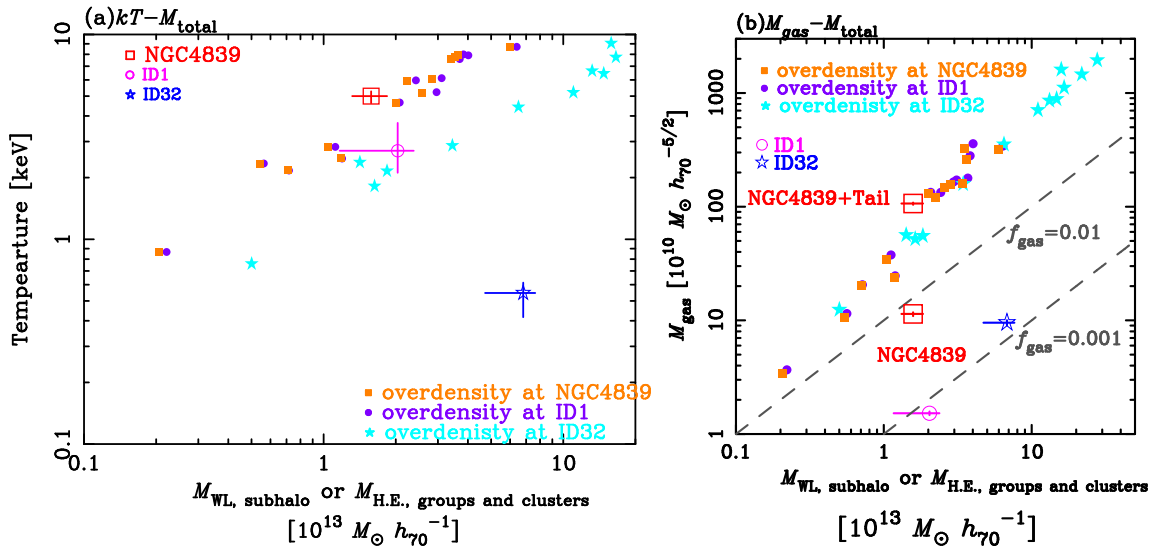


Fig. 14. (a) The temperature as a function of the gravitational mass. While the gravitational masses of the subhalos are the weak-lensing masses (Okabe et al. 2014), those of the groups are the hydrostatic masses computed using the temperature and density profiles derived by Vikhlinin et al. (2006). The open box indicates the subhalo associated with the NGC4839 group (this work). For comparison, the other subhalos labeled “ID1”, and “ID32” by Sasaki et al. (2015) are plotted with circles and stars, respectively. The filled boxes, circles, and stars show the temperature against hydrostatic mass for galaxy groups and clusters at the radius within which the mean densities of groups and clusters are equivalent to the overdensity of each subhalo within r_t . For details, see text. (b) The same as (a), but with gas mass against gravitational mass. (A color version of this figure is available in the online journal.)

$1.4 \times (n_{e,ICM}/2 \times 10^{-4} \text{ cm}^{-3})$, and the ram pressure could strip the gas associated with the subhalo. This result is well consistent with the X-ray tail morphology.

The gas mass in the “Tail” region was estimated to be approximately $1.0 \times 10^{12} M_{\odot}$ as described in section 4.3, and we assumed the gas was originally located within r_t before being stripped. Since the length of the X-ray tail is approximately $8 r_t$, the gas at the end of tail had been stripped approximately $400 \times (v/2000 \text{ km s}^{-1}) \text{ Myr}$ ago assuming a constant infall velocity. This value implies that mass-loss rate is approximately $2500 \times (v/2000 \text{ km s}^{-1})^{-1} M_{\odot} \text{ yr}^{-1}$. This value is comparable with those of merging groups in clusters (e.g., Eckert et al. 2014).

Nulsen (1982) estimated the mass-loss rate caused by turbulent stripped via Kelvin-Helmholtz instabilities; $\dot{M}_{KH} \approx \pi r^2 \rho_{ICM} v$. Here, r and ρ_{ICM} are the radius of the subhalo and gas density of the ICM, respectively. Since the mass-loss rate depend on the density profile of the ICM, we fitted the azimuthal average electron density profiles excluding the direction of the subhalo, “ID 9”, by Simionescu et al. (2013) with a β -model. We adopted the best-fit β -model profile out to the virial radius for calculation. Assuming that the groups was infalling from the virial radius of the Coma cluster and a constant infall velocity, $v = 2000 \text{ km s}^{-1}$, the timescale of the mass-loss was approximately 700 Myr. By integrating the mass-loss rate over the time scale, we obtained the total lost mass, $3 \times 10^{11} M_{\odot}$. If this gas had originally been within r_t , the gas mass fraction of the subhalo would be comparable with that of regular groups before infalling to the Coma cluster. The gas mass in the “Tail”

region is about three times greater than the lost mass via Kelvin-Helmholtz instabilities. This suggests that the ram pressure had been removed the gas more effective than Kelvin-Helmholtz instabilities.

5 Summary and conclusions

We observed the third massive subhalo “ID 9” detected from weak-lensing analysis (Okabe et al. 2014) with *Suzaku*. By comparing the subhalo mass distribution with thermodynamics obtained by X-ray observation, we first investigated cluster evolution through the accretion of objects.

While the X-ray peak is shifted approximately $1'$ away from the mass center, the NGC 4839 galaxy coincided with the X-ray peak. The X-ray tail was elongated toward the southwest direction or the outskirts of the Coma cluster, and the length was approximately $6 r_t$, $\sim 600 \text{ kpc}$. The temperatures of the central core and X-ray tail regions were approximately 5 keV. At a distance r_t toward the north, corresponding to the head of the subhalo, we found a temperature jump, from 5 keV to 8–10 keV. While the temperature of the southern part was also 7 keV at $1-2 r_t$, temperature profile beyond $2 r_t$ decreased to 4 keV. At $2 r_t$ in the southern part, we estimated a Mach number to be $\mathcal{M} = 1.73_{-0.16}^{+0.25}$ under the Rankine-Hugoniot condition. The gas mass fraction of the subhalo within r_t was approximately 0.7%. It is approximately 5 times smaller than that of regular groups and poor clusters. With the infall velocity estimated from the weak-lensing mass of the Coma cluster (Okabe et al. 2010), the ram pressure was comparable with the gravitational

force per unit area. Assuming the Kelvin-Helmholtz instabilities, the removed gas mass was estimated to be approximately $3 \times 10^{11} M_{\odot}$. Assuming that the removed gas had been within r_t before infalling to the Coma cluster, the gas mass fraction of the subhalo had been comparable with those of regular groups.

We thank the anonymous referee for careful reading the manuscript and providing valuable comments. We gratefully acknowledge all members of the *Suzaku* operation, calibration, and software development teams. TS is supported by JSPS Research Fellows. We acknowledge the support of Grants-in-Aid for Scientific Research from the MEXT, No. 25400235(K. M.), 25800112 (K. S.), and 26800097(N. O.). This work was supported by the Funds for the Development of Human Resources in Science and Technology under MEXT, Japan, and Core Research for Energetic Universe in Hiroshima University (the MEXT program for promoting the enhancement of research universities, Japan).

Appendix 1 Spectra of each region

Figure 15-20 show the other spectra extracted around the subhalo ‘ID 9’.

References

- Akamatsu, H., Inoue, S., Sato, T., Matsusita, K., Ishisaki, Y., & Sarazin, C. L. 2013, PASJ, 65, 89
- Akamatsu, H., & Kawahara, H. 2013, PASJ, 65, 16
- Akamatsu, H., van Weeren, R. J., Ogrea, G. A., Kawahara, H., Stroe, A., Sobral, D., Hoeft, M., Röttgering, H., Brügggen, M., et al. 2015, A&A, 582, A87
- Ascasibar, Y., & Markevitch, M. 2006, ApJ, 650, 102
- Ballarati, B., Feretti, L., Ficarra, A., Giovannini, G., Nanni, M., Olori, M. C., & Gavazzi, G. 1981, A&A, 100, 323
- Briel, U. G., Henry, J. P., & Boehringer, H. 1992, A&A, 259, L31
- Clowe, D., et al. 2006, ApJL, 648, L109
- Eckert, D., et al. 2014, A&A, 570, A119
- Ferrari, C., Govoni, F., Schindler, S., Bykov, A. M., & Rephaeli, Y. 2008, Space Sci. Rev., 134, 93
- Finoguenov, A., Sarazin, C. L., Nakazawa, K., Wik, D. R., & Clarke, T. E. 2010, ApJ, 715, 1143
- Ghizzardi, S., Rossetti, M., & Molendi, S. 2010, A&A, 516, A32
- Grevesse, N., & Sauval, A. J. 1998, Space Sci. Rev., 85, 161
- Gunn, J. E., & Gott, J. R., III 1972, ApJ, 176, 1
- Ichinohe, Y., Werner, N., Simionescu, A., Allen, S. W., Canning, R. E. A., Ehlert, S., Mernier, F., & Takahashi, T. 2015, MNRAS, 448, 2971
- Ishisaki, Y., Maeda, Y., Fujimoto, R., Ozaki, M., Ebisawa, K., Takahashi, T., Ueda, Y., Ogasaka, Y., Ptak, A., et al. 2007, PASJ, 59, 113
- Itahana, M., Takizawa, M., Akamatsu, H., Ohashi, T., Ishisaki, Y., Kawahara, H., & van Weeren, R. J. 2015, PASJ, 248
- Kuntz, K. D., & Snowden, S. L. 2008, A&A, 478, 575
- Kushino, A., Ishisaki, Y., Morita, U., et al. 2002, PASJ, 54, 327
- Leccardi, A., & Molendi, S. 2008, A&A, 486, 359
- Lodders, K. 2003, ApJ, 591, 1220
- Markevitch, M., et al. 2000, ApJ, 541, 542
- Markevitch, M., Gonzalez, A. H., David, L., Vikhlinin, A., Murray, S., Forman, W., Jones, C., & Tucker, W. 2002, ApJL, 567, L27
- Markevitch, M., & Vikhlinin, A. 2007, Phys. Rep., 443, 1
- Navarro, J. F., Frenk, C. S., & White, S. D. M. 1995, MNRAS, 275, 720
- Medezinski, E., Umetsu, K., Okabe, N., Nonino, M., Molnar, S., Massey, R., Dupke, R., & Merten, J. 2015, arXiv:1507.03992
- Neumann, D. M., et al. 2001, A&A, 365, L74
- Neumann, D. M., Lumb, D. H., Pratt, G. W., & Briel, U. G. 2003, A&A, 400, 811
- Nulsen, P. E. J. 1982, MNRAS, 198, 1007
- Ogrea, G. A., & Brügggen, M. 2013, MNRAS, 433, 1701
- Okabe, N., & Umetsu, K. 2008, PASJ, 60, 345
- Okabe, N., Okura, Y., & Futamase, T. 2010, ApJ, 713, 291
- Okabe, N., Bourdin, H., Mazzotta, P., & Maurogordato, S. 2011, ApJ, 741, 116
- Okabe, N., Futamase, T., Kajisawa, M., & Kuroshima, R. 2014, ApJ, 784, 90
- Okabe, N., Akamatsu, H., Kakuwa, J., Fujita, Y., Zhang, Y., Tanaka, M., & Umetsu, K. 2015, PASJ, 247
- Russell, H. R., Sanders, J. S., Fabian, A. C., Baum, S. A., Donahue, M., Edge, A. C., McNamara, B. R., & O’Dea, C. P. 2010, MNRAS, 406, 1721
- Russell, H. R., Fabian, A. C., McNamara, B. R., Edge, A. C., Sanders, J. S., Nulsen, P. E. J., Baum, S. A., Donahue, M., & O’Dea, C. P. 2014, MNRAS, 444, 629
- Simionescu, A., et al. 2013, ApJ, 775, 4
- Sasaki, T., Matsushita, K., Sato, K., & Okabe, N. 2015, ApJ, 806, 123
- Sasaki, T., et al., submitted to PASJ.
- Smith, R. K., Brickhouse, N. S., Liedahl, D. A., & Raymond, J. C. 2001, ApJL, 556, L91
- Struble, M. F., & Rood, H. J. 1999, ApJS, 125, 35
- Sun, M., Voit, G. M., Donahue, M., Jones, C., Forman, W., & Vikhlinin, A. 2009, ApJ, 693, 1142
- Taylor, J. E., & Babul, A. 2004, MNRAS, 348, 811
- Tormen, G., Moscardini, L., & Yoshida, N. 2004, MNRAS, 350, 1397
- Vikhlinin, A., Kravtsov, A., Forman, W., Jones, C., Markevitch, M., Murray, S. S., & Van Speybroeck, L. 2006, ApJ, 640, 691

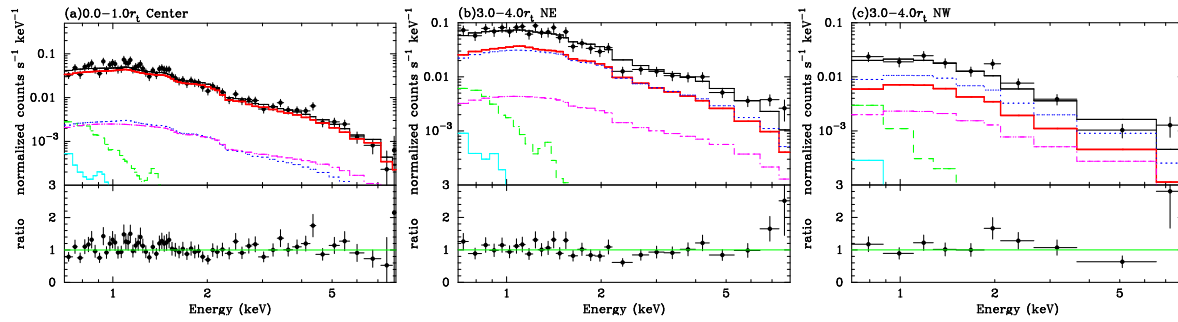


Fig. 15. The spectra in (a) “Center”, (b) $3-4 r_t$ in the “NE” sector, and (c) $3-4 r_t$ in the “NW” sector. The spectra were rebinned here for display purposes only. Upper panels show the NXB subtracted XIS 1 spectra (black crosses). The subhalo component is plotted as a (red) bold line. The ICM, CXB, LHB, and MWH components are indicated by (blue) dotted, (magenta) dash-dotted, (cyan) thin, and (green) dashed lines, respectively. The lower panels show the data-to-model ratios.

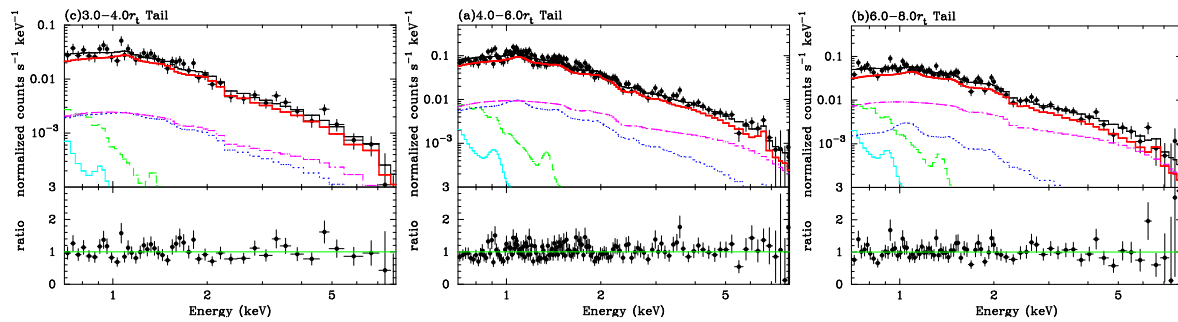


Fig. 16. The spectra of (a) $3-4 r_t$, (b) $4-6 r_t$, and (c) $6-8 r_t$ in the “Tail” sector. The spectra of $1-2 r_t$ and $2-3 r_t$ in this sector are shown in figure 5. The color notations are the same as figure 15.

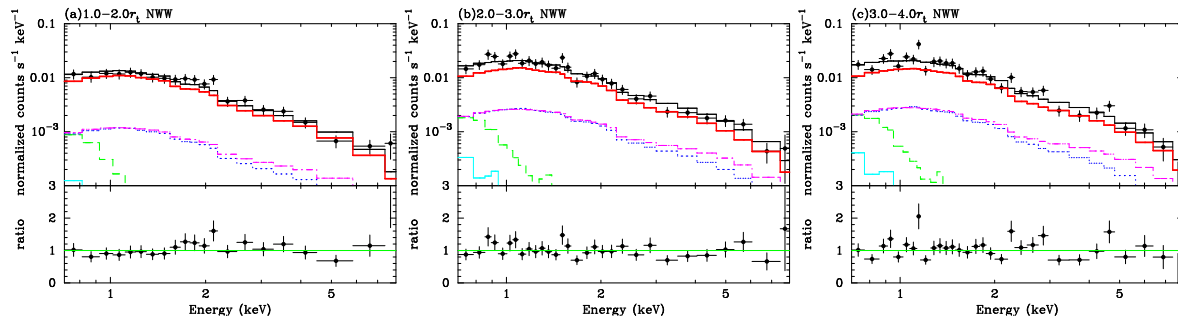


Fig. 17. The spectra of (a) $1-2 r_t$, (b) $2-3 r_t$, and (c) $3-4 r_t$ in the “NWW” sector. The color notations are the same as figure 15.

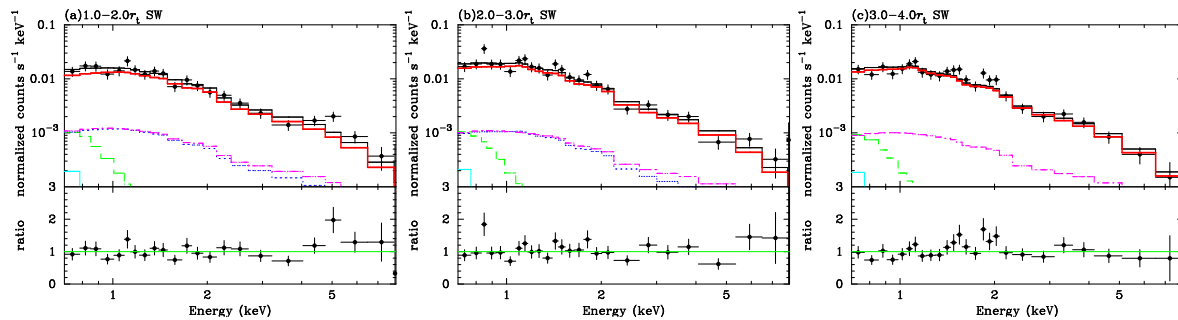


Fig. 18. The same as figure 15, but for the “SW” sector.

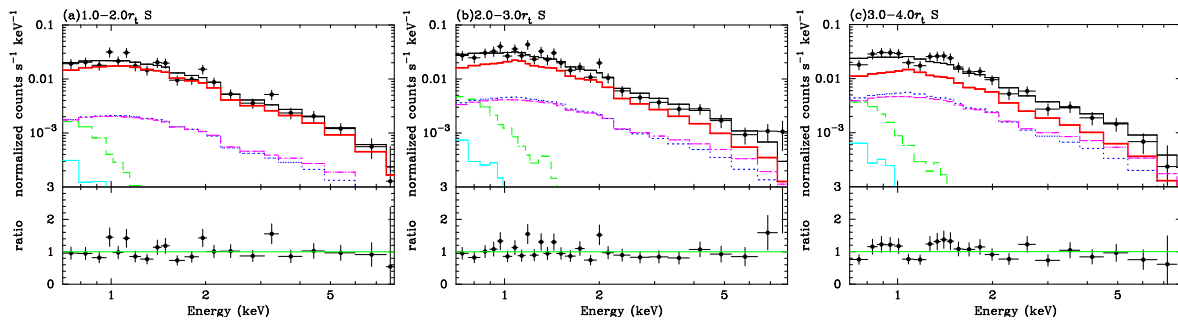


Fig. 19. The same as figure 15, but for the “S” sector.

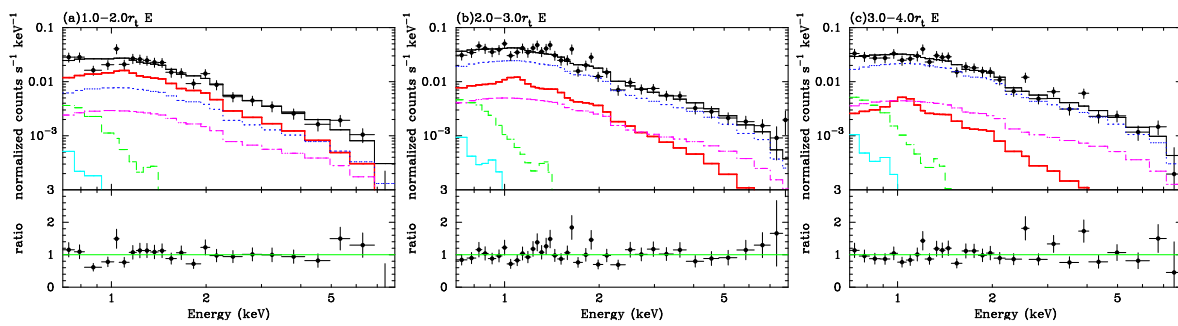


Fig. 20. The same as figure 15, but for the “E” sector.